



Microstructural Evolution and Mechanical Behavior of Additively Manufactured 316 L Subjected to Varied Deformation Directions

X. He¹ · B. B. He¹

Received: 9 February 2023 / Accepted: 26 May 2023 / Published online: 17 June 2023
© The Author(s) under exclusive licence to The Korean Institute of Metals and Materials 2023

Abstract

The present work investigates the effect of deformation directions on the microstructure and mechanical properties of 316 L stainless steel processed by additive manufacturing (AM). It is found that crossly rolled AM 316 L after thickness reduction of 10% demonstrates an enhanced density of deformation twins along the different directions and a substantial hardness increment (108.6 HV, ~48.5%). The cross rolling process effectively raises the twinning Schmid factors, the fraction of grains in high twinning Schmid factor regions and activates the generation of multiple twinning systems. The deformation twins with multiple twinning systems have a better capacity in storing the dislocations than that with single twinning system during deformation. Thus, the large increment of hardness after small deformation using cross rolling can be ascribed to increased dislocation and twin densities while the elevated dislocation density is also assisted by the presence of multiple deformation twins. The present work suggests that the multiple deformation twinning of austenitic steel with hierarchically heterogeneous microstructure processed by AM can be effectively activated under small deformation of cross rolling, which may be also applicable for other face centered cubic metallic materials with low stacking fault energy.

Keywords Multiple deformation twins · Dislocations · Cross rolling · Additive manufacturing · 316L stainless steel

1 Introduction

Additive manufacturing (AM) process, has drawn enormous attention during the last decades due to the ability of near net-shape manufacturing of complex-shaped components [1]. Laser powder bed fusion (L-PBF) as a useful laser-based AM process has been used to manufacture components of many alloys, such as AlSi10Mg, Inconel 718, TiAl-based alloys, and stainless steels [2]. Austenitic stainless steel 316 L are widely used in different engineering sectors due to their high work-hardening behavior, good formability, and excellent corrosion resistance [3]. Many 316 L products have complex shapes, including various tailor-made implants [4], structural components for the aerospace and automotive industries [5], and pipeline systems for the

nuclear industry [6], making conventional production procedures costly and difficult. Fortunately, a promising result is that 316 L components made using L-PBF may even have superior mechanical properties (higher strength and equivalent ductility) than their cast and even wrought counterparts [7]. Thus, there is enormous potential in production of 316 L components using AM processes, and it is crucial to understand the connection between AM microstructure and mechanical properties.

It is reported that the metallic material with low stacking fault energy (SFE) such as austenitic stainless steel deformed at low temperature and high strain rate is prone to produce intense deformation twins [8], resulting in reduced twin thickness and thus higher strength [9]. The twin boundary (TB) can effectively block the motion of dislocations and thus increases the strength of austenitic stainless steel [10, 11]. More interestingly, the presence of a TB may not impair the tensile ductility as the dislocations can dissociate and glide on the TB [10]. However, the plasticity in austenitic stainless steels under ambient environment and quasi-static strain rate generally initiates with dislocation slipping at early stages, followed by the formation of extensive stacking faults (SFs). The stage where deformation twinning

✉ X. He
hex2020@mail.sustech.edu.cn

✉ B. B. He
hebb@sustech.edu.cn

¹ Department of Mechanical and Energy Engineering,
Southern University of Science and Technology,
Shenzhen 518055, China

dominates the deformation mechanism of austenitic stainless steels is usually at a large strain level [12, 13].

It has been shown that the predominant inhomogeneous deformation resulting from the hierarchically heterogeneous microstructures leads to stress concentrations and provides ample nucleation sites for deformation twins [14]. Interestingly, the biaxial strain path generally induces an increased amount of deformation twins owing to the dependence of deformation twinning on the strain path [15, 16]. Thus, the present work investigates the deformation twinning behavior of 316 L with hierarchical heterogeneous microstructure processed by AM via unidirectional and cross rolling. It is found that high-density multiple deformation twins can be introduced into the hierarchically heterogeneous microstructures of AM 316 L by cross rolling under small deformation of only 10% thickness reduction and accompanied with an increase of strength.

2 Experiments

2.1 Materials and Processing

The 316 L stainless steel powders (15–55 μm) with a nominal chemical composition of Fe-18Cr-13Ni-2.3Mo-0.8Mn-0.7Si in wt% are produced by Oerlikon Metco Inc. The AM 316 L is processed via L-PBF (DiMetal-100 H, 200 W, 40 μm beam diameter) with laser power, scan rate, hatch spacing, and layer thickness of 200 W, 283 mm/s, 300 μm , and 30 μm , respectively. The rotational scanning with an angle between each layer of 67° is used to obtain microstructure with relatively low texture and isotropic mechanical properties [17]. For comparison purpose, the as-built (AB) 316 L sample is subjected to annealing at 1200 $^\circ\text{C}$ for 1 h to obtain a fully recrystallized microstructure [18], which is termed as HT sample hereafter. The AB and HT samples are deformed by unidirectional rolling (UR) and cross rolling (CR), which are marked as ABU, ABC, HTU, and HTC for brevity. The ABU samples are prepared with the building direction parallel to the rolling direction. For CR process, the workpiece is rotated by 90° in the rolling plane after each rolling pass. The AB sheets are rolled unidirectionally and crossly with thickness reductions of 10%, 30%, and 50% at room temperature. The thickness reduction per rolling path is $\sim 100 \mu\text{m}$, which represents a thickness reduction of $\sim 2.5\%$ in each pass. The HT sheets are unidirectionally and crossly rolled with thickness reductions of 10% and 50% at the same rolling condition for comparison purpose.

2.2 Structure Characterization

The samples for microstructure characterization and neutron diffraction tests are prepared through the electropolishing

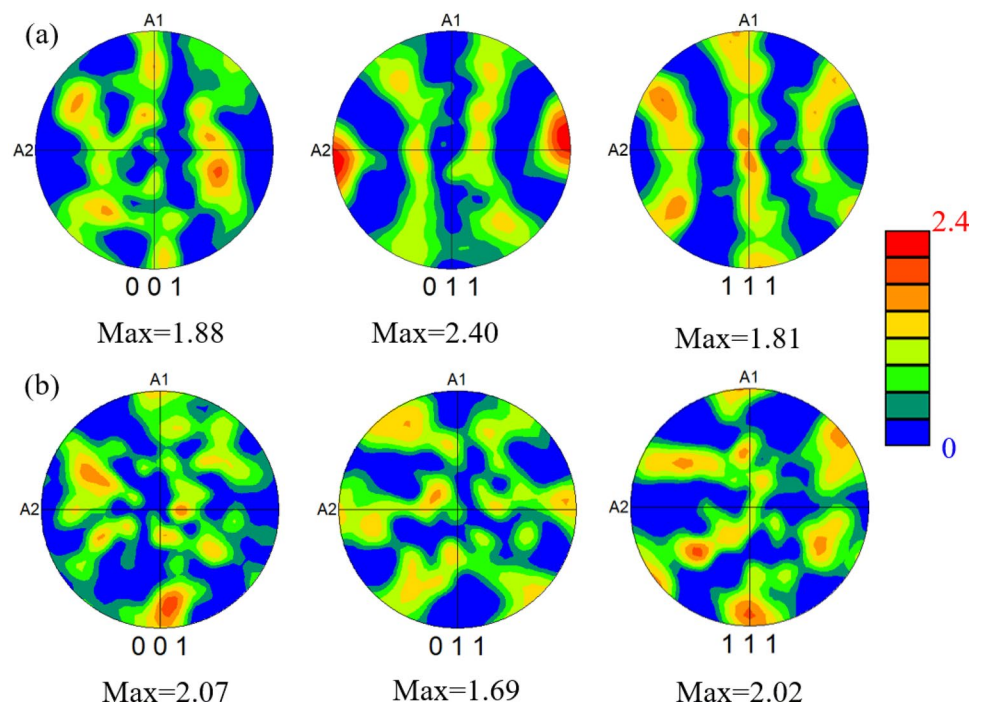
technique in a solution of 10% perchloric acid and 90% ethanol (vol%) at room temperature. The Vickers hardness of samples is measured with a maximum load of 200 gf and a dwell time of 10 s. Each hardness value is averaged from at least six measurements. The initial microstructure is captured by the scanning electron microscope (SEM, Merlin, ZEISS) equipped with an electron backscatter diffraction detector (EBSD, Digiview4, EDAX Inc.). For EBSD data collection, an accelerating voltage of 20 kV and a current of 5 nA are used. Neutron diffraction characterization is carried out using a deep-penetrating neutron beam with high spatial resolution and intensity, making it suitable for analysis of complex anisotropic structures [19]. The diffraction profile information of the deformed steels is estimated with a 360° rotation stage on a General-Purpose Powder Diffractometer (GPPD) at China Spallation Neutron Source (CSNS). The time-of-flight (TOF) method is used to collect data with a total scanning time of 1 h. Standard strain-free Si powders are used to eliminate instrumental errors.

3 Results

The (001), (011), and (111) EBSD pole figures of the specimen are illustrated in Fig. 1. All the pole figures exhibited low multiples of random distribution (MRD) intensities, indicating that both AB and HT specimens did not have strong crystallographic texture. Additionally, the AB sample shows a relatively higher (011) texture along the building direction with a maximum intensity of MRD of about 2.40 (Fig. 1a). The intensity along the (001) and (111) directions is weaker as compared to that along (011) direction (Fig. 1a). As compared to the AB sample, the HT sample has higher (001) and (111) texture with maximum MRD intensity of 2.07 and 2.02, respectively.

Figure 2a and b show that the AB and HT samples both have an inhomogeneous distribution of grain size. The average grain size is characterized by line-intercept method with grain diameter of $\sim 16 \mu\text{m}$ and $\sim 38 \mu\text{m}$ for AB and HT samples, respectively. The phase maps together with TBs, low and high angle grain boundaries (LAGBs and HAGBs) in the AB sample (Fig. 2c) are sharply different from those of HT sample (Fig. 2d). Additionally, some annealing twins are observed in the HT sample (Fig. 2d), with spacing ranging from several to dozens of micrometers, whereas such twins are seldom observed in the AB sample. The Kernel average misorientation (KAM) map shows that the AB sample has a higher misorientation near the LAGBs and HAGBs than the HT sample, indicating a higher density of geometrically necessary dislocations (GNDs). The higher GND density could result from the compression-tension cycles rendered by the localized thermal history upon laser scanning [20]. Figure 2 g and

Fig. 1 The (001), (011), and (111) pole figures of the **a** AB and **b** HT samples. The original EBSD data in Fig. 2 are rotated in the way that ND lies at the center of the pole figures



h shows the grain orientation spread (GOS) of AB and HT sample, respectively. The GOS gives a quantitative description of the crystallographic orientation gradients in individual grains [21]. The GOS value of the AB sample is much higher than that of the HT sample due to the residual stress introduced during L-PBF process. By applying the GOS threshold value of 1.5° [22], the volume fraction of recrystallized and non-recrystallized grains in the HT sample is 53.6% and 46.4% respectively. Additionally, the maximum GOS value of HT sample is 4.69° , which is below the GOS threshold value of recovery (6°) [22], thus the non-crystallized fraction are fully recovered substructures.

Figure 3a shows that the hardness of samples increases with decreased sample thickness. The ABC sample has a higher hardness than that of the ABU sample, while the opposite trend is found in the HT samples. The hardness increases rapidly at the first 10% thickness reduction in all samples and is followed by a gradual increment at the subsequent rolling thickness reduction, and finally reach a similar value of hardness at a thickness reduction of 50%. Interestingly, the ABC sample under a small thickness reduction (10%) demonstrates a high hardness of 332.7 HV, which is about 48.5% higher than that of the AB sample (224.1 HV). In contrast, the increment of hardness for the ABU, HTU, and HTC samples are found to be 63.1, 89.9, and 77.9 HV, respectively. The high hardness and the corresponding hardness increment of the ABC sample at the first 10% thickness reduction suggests that there

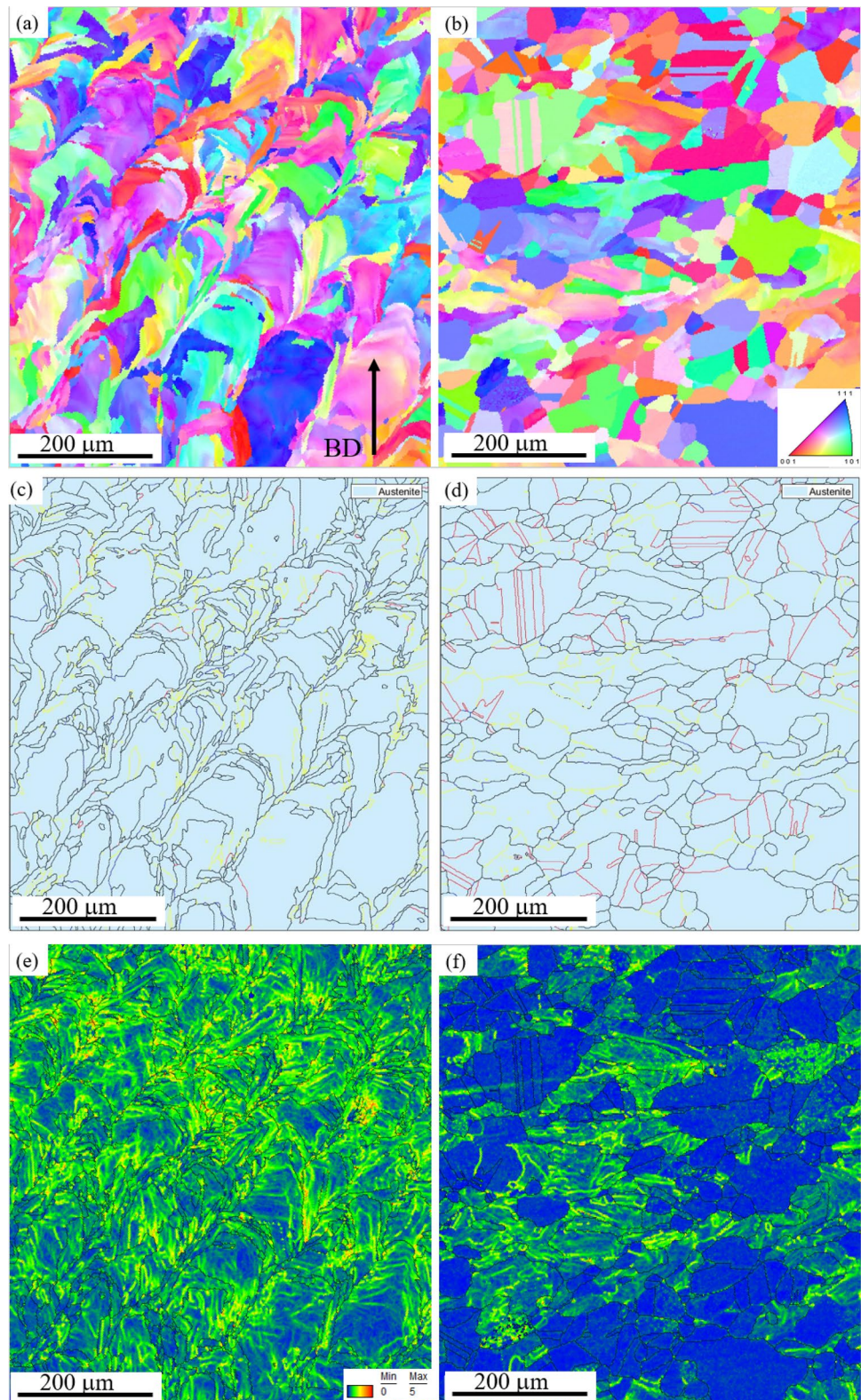
may exists some different deformation mechanisms during deformation of the AB sample by cross rolling.

Figure 4a-f are the superimposed EBSD image quality (IQ) and IPF maps depicting the typical microstructures of the AB samples with different thickness reduction under CR and UR. The deformation twins can be revealed by the band contrast as lines with a grey level distinguishable from the matrices [23]. Intensive deformation twins are observed in the ABC (Fig. 4a-c, g) and ABU (Fig. 4d-f, h) samples. The amount of deformation twins increases with decreased sample thickness. Additionally, at a thickness reduction of 10%, the deformation twins in the ABC sample generally demonstrate multiple twinning systems with formation of intersecting twin boundaries (Fig. 4a and g), which are sharply different from the ABU sample that single twinning system is dominated (Fig. 4d and h).

Different from the deformed AB samples with a high density of twins, sporadically distributed twins are observed in the HTC (Fig. 5a) and HTU (Fig. 5c) samples with a thickness reduction of 10%. Since the HT samples are the recrystallized state of AB samples, both samples should have a similar chemical composition. Thus, the difference in the formation of deformation twins in the present two samples should be due to the deformation process and the substructure resulting from the AM process.

The EBSD KAM maps of the deformed AB and HT samples with different thickness reduction ratio under CR and UR are shown in Figs. 6 and 7, respectively. The KAM level of the ABC sample is much higher than that of the

Fig. 2 The EBSD inverse pole figure (IPF) of **a** AB and **b** HT samples, the building direction (BD) of the LPBF process is marked by a black arrow. The EBSD band contrast map shows the distribution of boundaries in **c** AB and **d** HT samples. Gray color: Face centered cubic phase. The red, yellow, and black lines respectively indicate the TBs, LAGBs, and HAGBs. The KAM map of **e** AB and **f** HT samples. The grain orientation spread (GOS) of the **g** AB and **h** HT sample. (For interpretation of the references to color in this figure legend, the reader is referred to the web version of this article.)



other samples at the same deformation stage. For quantitative investigation, the average GND density of the undeformed and 10% deformed samples is calculated from the KAM data by using the equation $\rho_{GND} = \lambda\theta/Xb$ [24], where

$\lambda = 2$ (for low angle tilt boundaries), θ is the average local misorientation angle, $X = 0.8 \mu\text{m}$ is the step size for EBSD data collection, and $b = 0.254 \text{ nm}$ is the magnitude of Burgers vector for 316 L stainless steel. Using the equation,

Fig. 2 (continued)

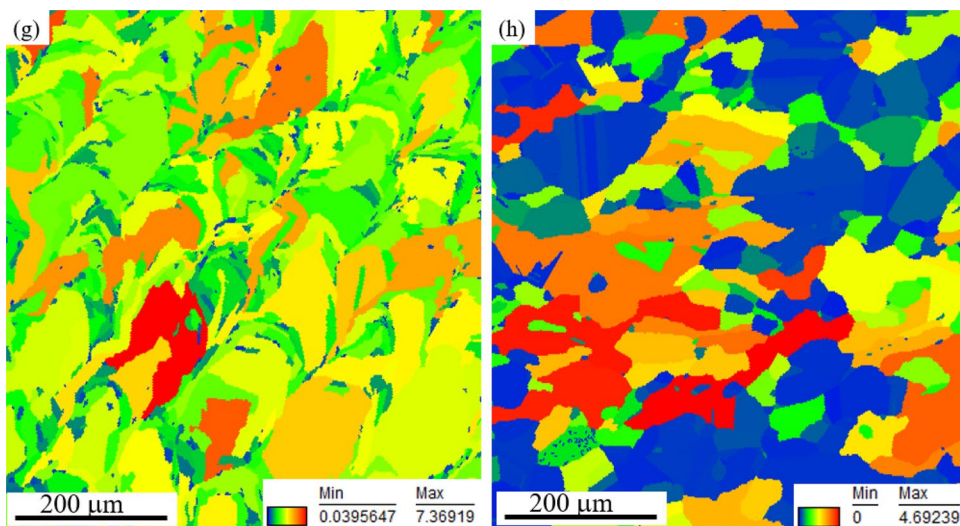
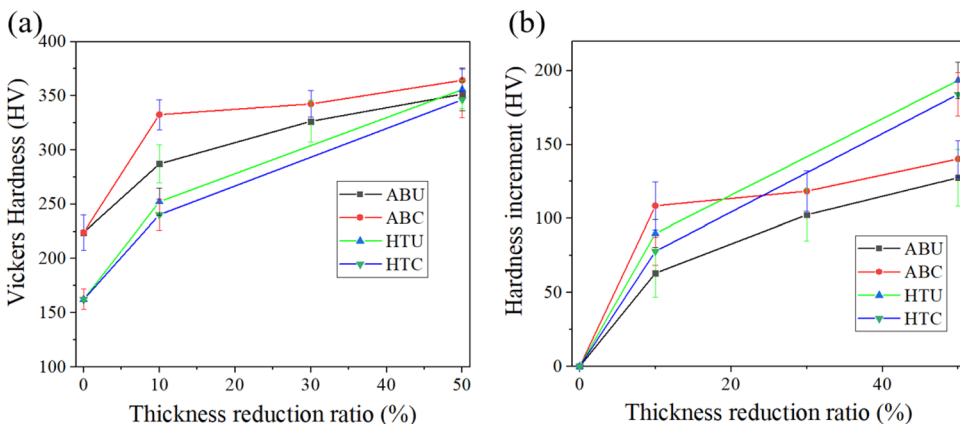


Fig. 3 The **a** Vickers hardness and **b** hardness increment of AB and HT samples after UR and CR experiments with different amount of thickness reductions. Error bar represents the standard deviation of at least 6 tests



we plot the average GND density value and increment of the 10% deformed samples in Fig. 8. The GND density of the 10% deformed ABC sample is $3.49 \times 10^{14} \text{m}^{-2}$, which is much higher than that of the ABU sample ($2.26 \times 10^{14} \text{m}^{-2}$), whereas the difference between HTU ($1.28 \times 10^{14} \text{m}^{-2}$) and HTC sample ($1.10 \times 10^{14} \text{m}^{-2}$) is marginal.

Neutron diffraction (ND) experiments are carried out to capture the evolution of defects in the samples with different thickness reductions. The modified Williamson–Hall (mW-H) method is employed for the semi-quantitative calculation of dislocation density. The peak fitting is performed by using the Fityk software package [25] with pseudo-Voigt function, which allows the determination of full width at half maximum (FWHM) and peak position. Figure 9a shows the fitted profile of the AB 316 L after cross-rolling with 10% thickness reduction. According to the mW-H method, the broadening of the diffraction peaks is a function of the average crystallite size D_l (i.e., the average coherent scattering domain size), the dislocation density ρ , and faulting probability as described by the following Eqs. [26, 27]:

$$\Delta K - \beta W_{hkl} = 0.9/D_l + (\pi A^2 b^2/2)^{1/2} \cdot \rho^{1/2} \cdot K C^{-1/2} + O(K^2 C) \tag{1}$$

where b represents the magnitude of the Burgers vector, K and ΔK are the exact Bragg position and FWHM, respectively. O is the high order term in $K^2 C$, which is neglected for calculation. $\beta = (1.5\phi_s + \phi_t)/a_0$, where a_0 is the lattice constant (0.35967 nm for 316 L [28]), ϕ_s and ϕ_t are the probability to find a SF and a TB in $\{111\}$ planes, respectively. A is a constant depending on the effective outer cutoff radius of dislocations. $A < 1$ stands for highly correlated dislocation arrangement and $A > 1$ for random arrangement [29]. The value of A indicates the extent of the dipole character (i.e., strain field) of dislocations but does not reflect either the coherently scattering crystallite size or the distance between dislocations [30]. It has been reported that by taking $A = 1$, the best fit convergence was obtained although other A -values up to 2 yielded similar dislocation densities [31]. Thus, in this work for semi-quantitative dislocation density calculation, the value of A is taken as 1 for all the specimens.

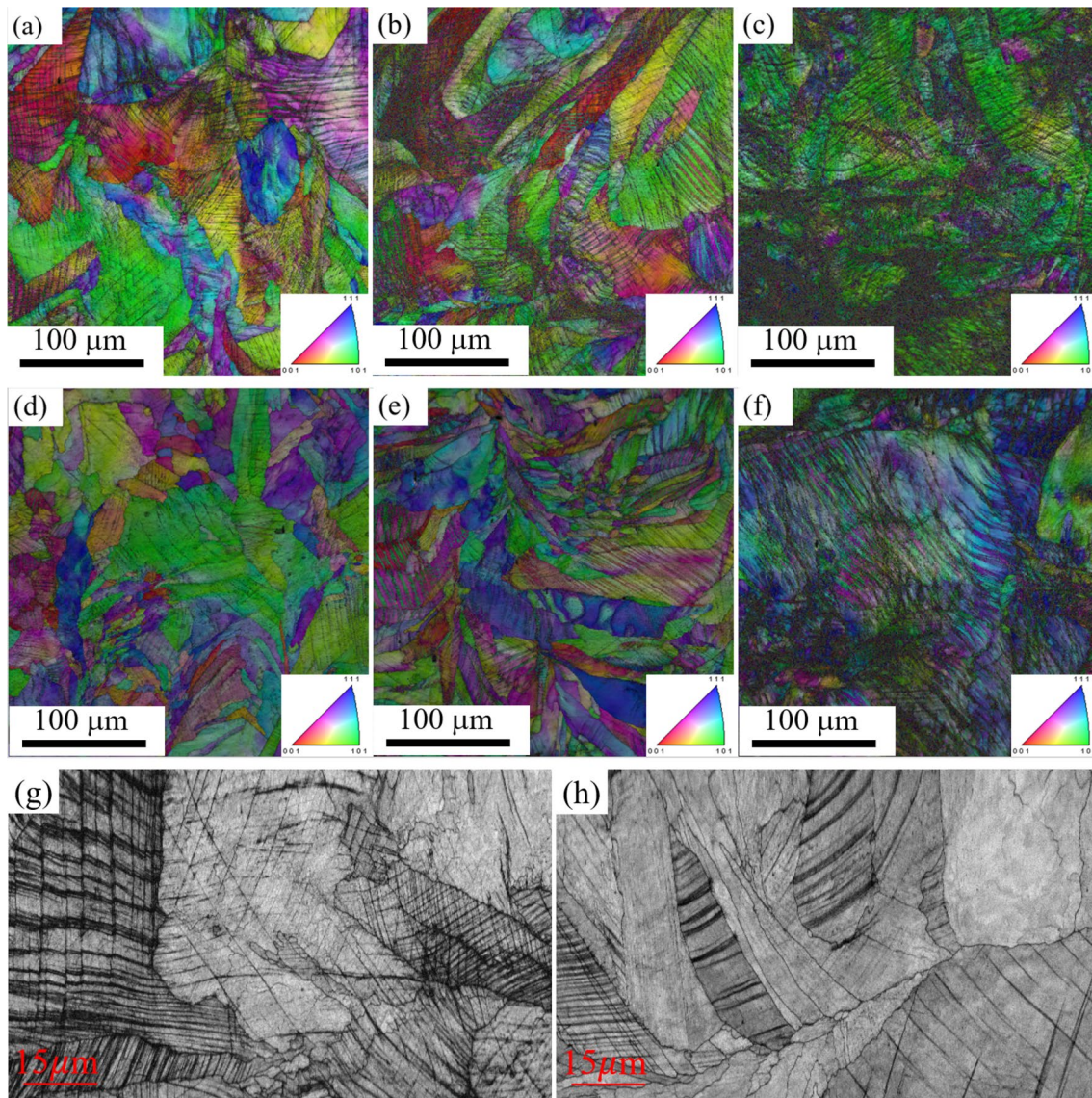


Fig. 4 The superimposed EBSD IQ+IPF map of the **a-c** ABC and **d-f** ABU samples with thickness reduction ratio of **a, d** 10%, **b, e** 30%, and **c, f** 50%, respectively. **g, h** The magnified view of the deformation twins in the **g** ABC and **h** ABU samples with a reduction of 10%

W_{hkl} is a factor used to scale the peak broadening induced by faulting at different $\{hkl\}$ reflections [32]. The W_{hkl} values at different reflections in face centered cubic materials have been estimated previously in [32]. C is the average dislocation contrast factor, which can be determined for each $\{hkl\}$ reflection by the following equation [33]:

$$\bar{C} = \bar{C}_{h00} (1 - qH^2), \quad H^2 = (h^2k^2 + k^2l^2 + h^2l^2)/(h^2 + k^2 + l^2)^2 \quad (2)$$

where \bar{C}_{h00} and q are constants depending on the anisotropic elastic constants C_{11} , C_{12} , C_{44} , and can be determined by [33]:

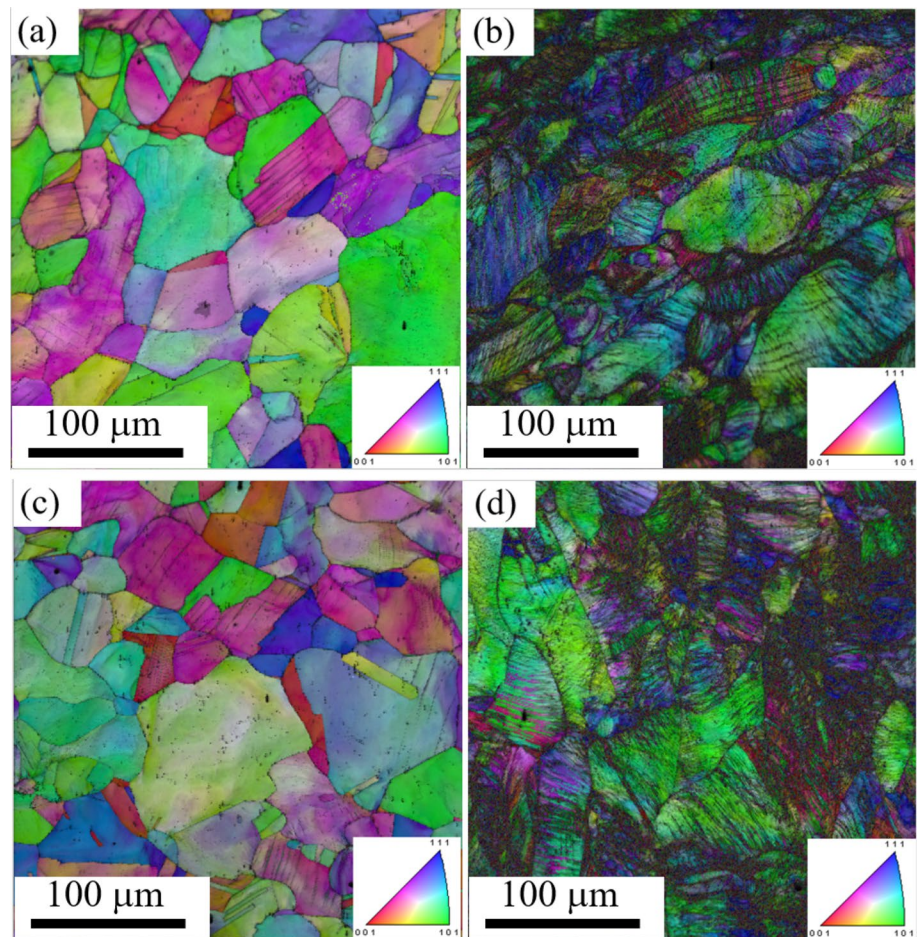
$$\bar{C}_{h00} = a[1 - \exp(-A_i/b)] + cA_i + d \quad (3)$$

$$q = a[1 - \exp(-A_i/b)] + cA_i + d \quad (4)$$

where, $A_i = 2C_{44}/(C_{11} - C_{12})$ is the elastic anisotropy. Parameters to calculate \bar{C}_{h00} and q in 316 L crystal using C_{11} , C_{12} , and C_{44} as 210 GPa, 130 GPa, and $C_{44}=120$ GPa, respectively [17, 34], and other parameters are listed in Table 1 [33].

In this study, the AB and HT samples deformed by UR and CR are chosen for the neutron diffraction peak profile analysis. Seven peaks including (111), (200), (220), (311), (222), (331), and (420) are recorded for each line profile.

Fig. 5 The superimposed EBSD IQ + IPF map of the **a, b** HTC and **c, d** HTU samples with thickness reduction ratio of **a, c** 10%, and **b, d** 50%, respectively



With the values of K and ΔK determined from the experiments, Dl , ρ , and β are obtained from the best linear fitting between $\Delta K - \beta W_{hkl}$ and $K C^{-1/2}$, as the mW-H plot of the ABC sample with a thickness reduction of 10% as shown in Fig. 9b.

The dislocation density of samples increases with reduced sample thickness (Fig. 9c). At the thickness reduction of 50%, the ABC sample has the highest dislocation density of $1.63 \times 10^{15} m^{-2}$, and the other three samples had a similar dislocation density of $1.39 \times 10^{15} m^{-2}$. At the thickness reduction of 10%, the HTU sample has higher dislocation densities than that of the HTC sample (Fig. 9c). Whereas, at the same thickness reduction, the dislocation density of the ABC sample is much higher than that of the ABU sample. The increment of dislocation density from thickness reduction of 30%–50% of the ABU sample is markedly lower than that of the ABC 316 L sample.

The average crystallite size of samples decreased with reduced specimen thickness reduction as shown in Fig. 9d. The initial crystallite sizes of the AB and HT samples calculated from neutron diffraction profile is $\sim 0.5 \mu m$ and $\sim 60 \mu m$, respectively, which is coincident with the coherent

scattering domain size, i.e., average cell size of AB sample and the average grain size of HT sample. At the thickness reduction of 50%, the average crystallite sizes of the AB and HT samples come to a similar value of $\sim 160 nm$. The faulting probability ($1.5\phi_s + \phi_t$), including the contribution from deformation SFs and twins, increases with decreased sample thickness (Fig. 9e). The faulting probability can be viewed as twin density by regarding the stacking fault probability as a small twinning probability [35]. The ABC sample possesses the highest twin density (Fig. 9e). The twin density of the CR samples is higher than that of the UR samples. The HTC sample with a thickness reduction of 10% steel has a lower twin density than that of ABU sample, which is qualitatively consistent with the EBSD observation (Figs. 4 and 5).

4 Discussion

Based on the detailed microstructure observation (Figs. 4 and 5), it is found that the twinning activity is substantially enhanced in the AB 316 L after the cross rolling process. Deformation twinning is an orientation-dependent mechanical behavior in metallic materials. As a polycrystalline metal

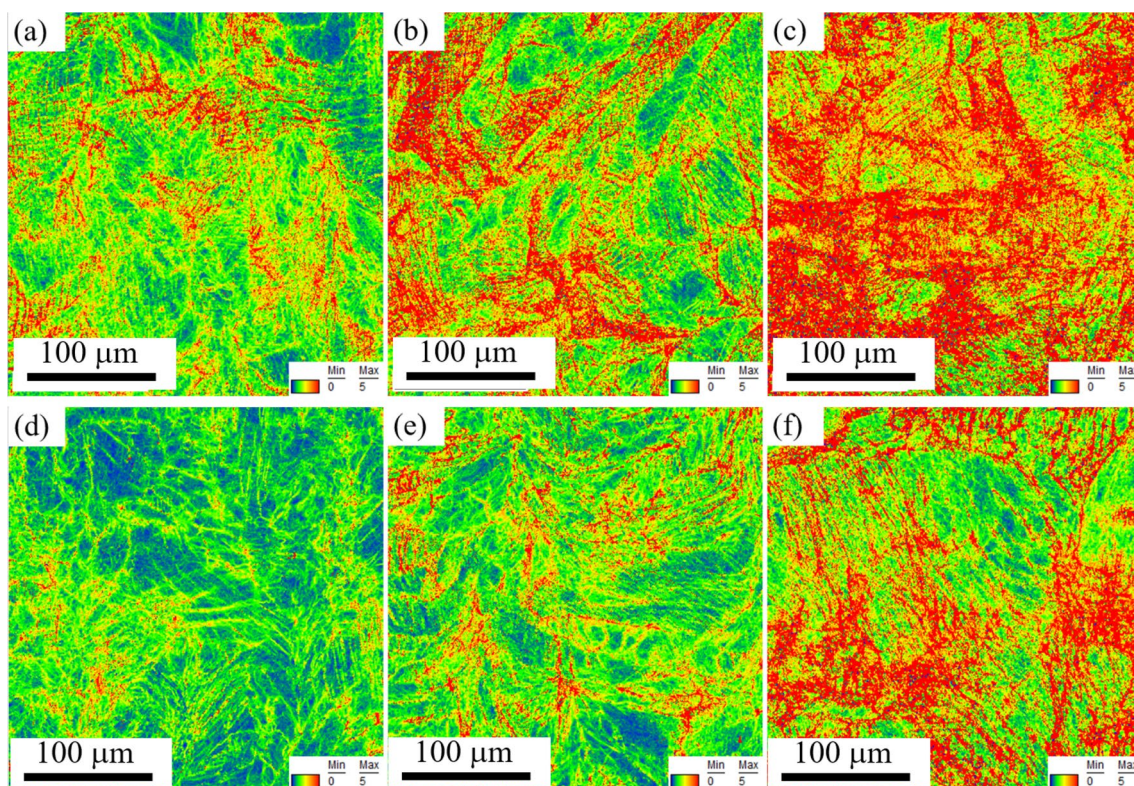


Fig. 6 The EBSD KAM map of the **a-c** ABC and **d-f** ABU samples with thickness reduction ratio of **a, d** 10%, **b, e** 30%, and **c, f** 50%, respectively

with randomly oriented grains, deformation twins may form only in a fraction of grains with favorable orientations [36], whereas other grains are deformed by dislocation activities, forming dislocation cells or tangles. To reveal the enhanced deformation twinning by cross rolling at a low strain regime, the twinning Schmid factors for all grains in Fig. 2a are analyzed. The twinning Schmid factors (m_t) under rolling are calculated by using the formula [16, 37]:

$$m_t = 0.5 \times (\cos\alpha\cos\beta - \cos\gamma\cos\delta) \quad (3)$$

where, α , β represent the angles between rolling direction and twinning system, and γ , δ are angles between normal direction and twinning system, respectively.

Figure 10a and b show the Schmid factors to $(111)[\bar{1}12]$ twinning system under UR and CR, respectively. In general, the FCC structure has twelve twinning systems. Figure 10c and d show grain frequencies of Schmid factors to twinning systems under UR and CR, respectively. A total shift of twinning Schmid factors from low-value regions under UR to medium-value regions under CR is also included. The twinning systems have more grains in high-value regions in CR conditions as compared to the UR conditions (Fig. 10c and d). Figure 10e shows average Schmid factors to twinning systems under UR and CR conditions. As it shows, the

CR process increases average Schmid factors for all twinning systems. For a twinning system in one grain under the UR process, it only has one Schmid factor. In contrast, the single twinning system has two independent Schmid factors corresponding to two orthogonal rolling directions under the CR process. Thus, the twinning systems can have more chances to get a high Schmid factor under CR conditions [16]. Nevertheless, the $(111)[112]$, $(111)[121]$, and $(111)[\bar{1}12]$ twinning systems under both UR and CR conditions possess high average Schmid factors (Fig. 10e), suggesting that these three twinning systems are easier to be initiated in 316 L under the different rolling conditions.

It has been reported that the amount of twinning systems activated in an individual grain is less than four [16]. Thus, the top four largest average twinning Schmid factors (noted as 1st, 2nd, 3rd, and 4th) under rolling condition are analyzed to understand the multiple twinning behaviors in the present 316 L. The top four largest average twinning Schmid factors of all grains in Fig. 2a are screened out. The average twinning Schmid factors of 1st – 4th are illustrated in Fig. 11a. Grains in CR samples have higher top four largest average twinning Schmid factors than that in UR samples (Fig. 11a). Moreover, the 4th largest average twinning Schmid factor for CR condition is even larger than the 1st largest average twinning Schmid factor for UR condition

Fig. 7 The EBSD KAM map of the **a, b** HTC and **c, d** HTU samples with thickness reduction ratio of **a, c** 10%, and **b, d** 50%, respectively

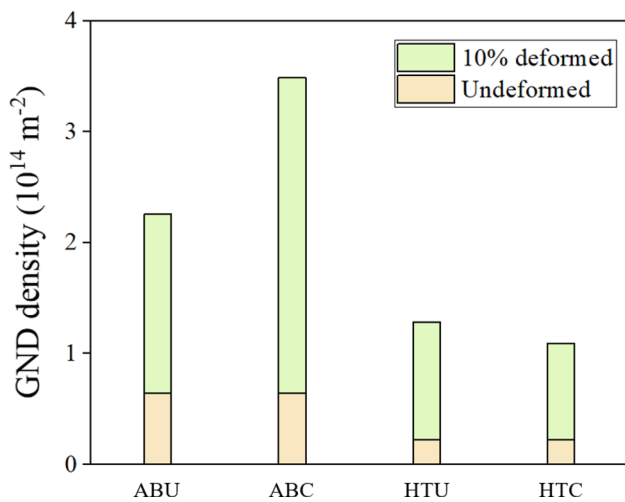
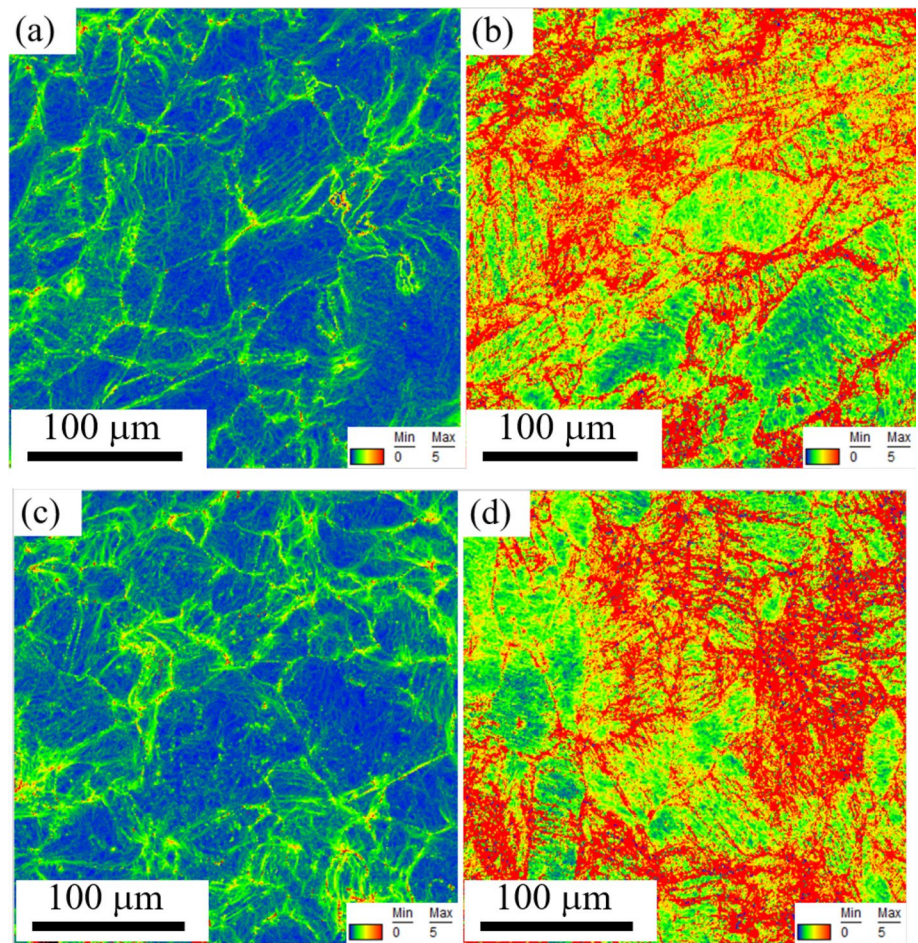


Fig. 8 The average GND density value and increment of the samples with 10% rolling deformation

(Fig. 11a). The grain frequency distributions to twinning Schmid factor are narrowing with high frequency for the top three largest average twinning Schmid factors under CR condition (Fig. 11b), which are not observed in UR, indicating

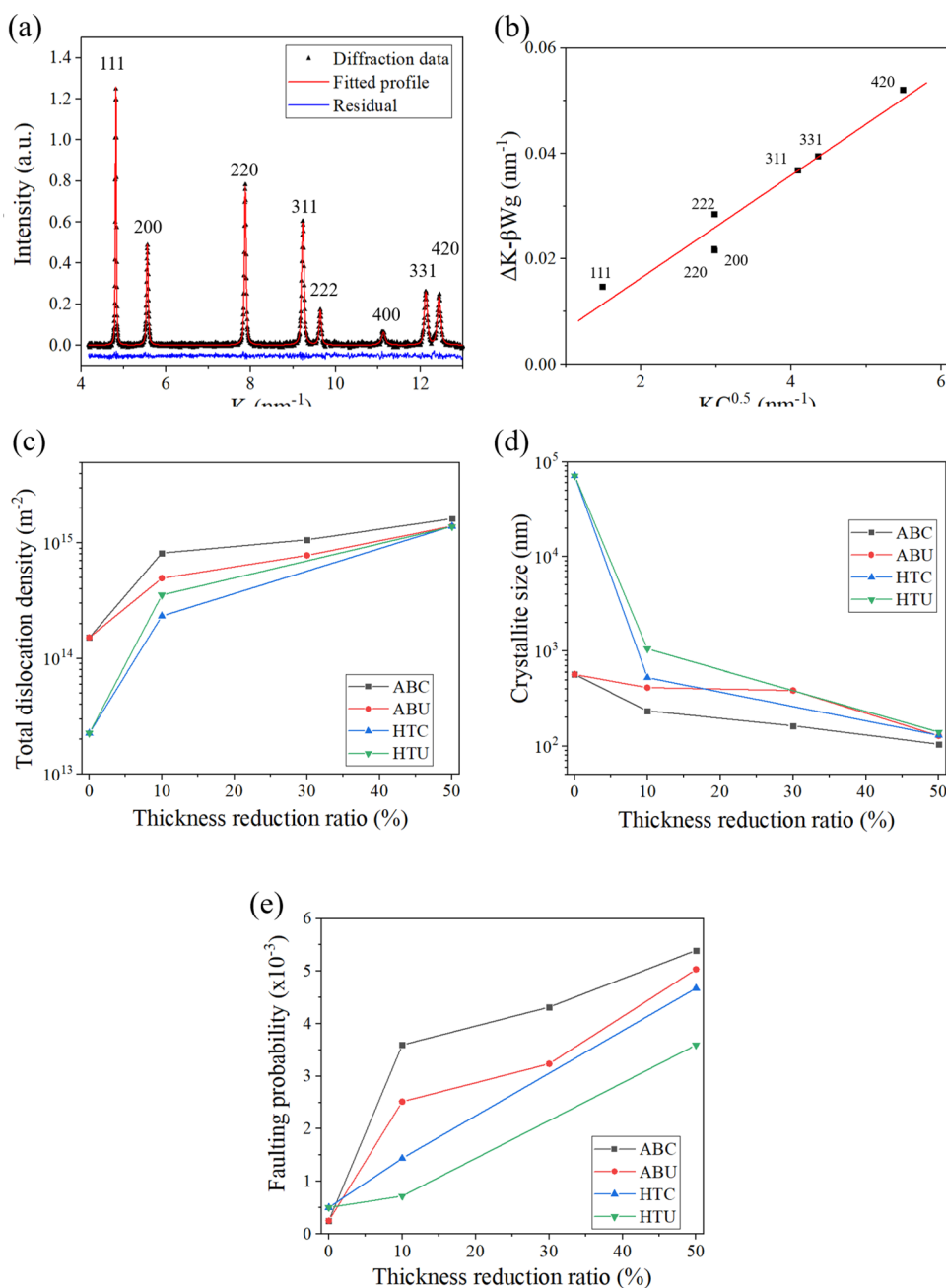
Table 1 The value of different parameters employed to calculate \bar{C}_{h00} and q in 316 L

Parameters	q		\bar{C}_{h00}	
	Screw	Edge	Screw	Edge
a	5.4252	4.8608	0.174	0.1687
b	0.7196	0.8687	1.9522	2.04
c	0.069	0.0896	0.0293	0.0194
d	-3.197	-3.428	0.0662	0.0926

that CR condition can improve the top four largest average twinning Schmid factors distributions and promoting the formation of multiple deformation twinning along different direction (Figs. 4 and 5).

Generally, deformation twins are initiated from GB where the accumulated stress at the GB provides a driving force to induce deformation twinning [38–40]. It has been reported that the nano twins are initiated from the dislocation cell boundaries (CBs) in AB 316 L instead. This is because the CBs could also emit and trap partial dislocations, making the formation of deformation twins through the glide of partial dislocations on the adjacent planes possible [7]. Following

Fig. 9 The **a** measured and fitted neutron diffraction profiles and **b** modified Williamson-Hall plot of ABC sample with a thickness reduction of 10%. The difference between the experiment and the fitting curve in **a** is displayed at the bottom of the figure. The **c** dislocation density, **d** average crystallite size, and **e** faulting probability of AB and HT samples at different thickness reductions are obtained from the UR and CR experiments

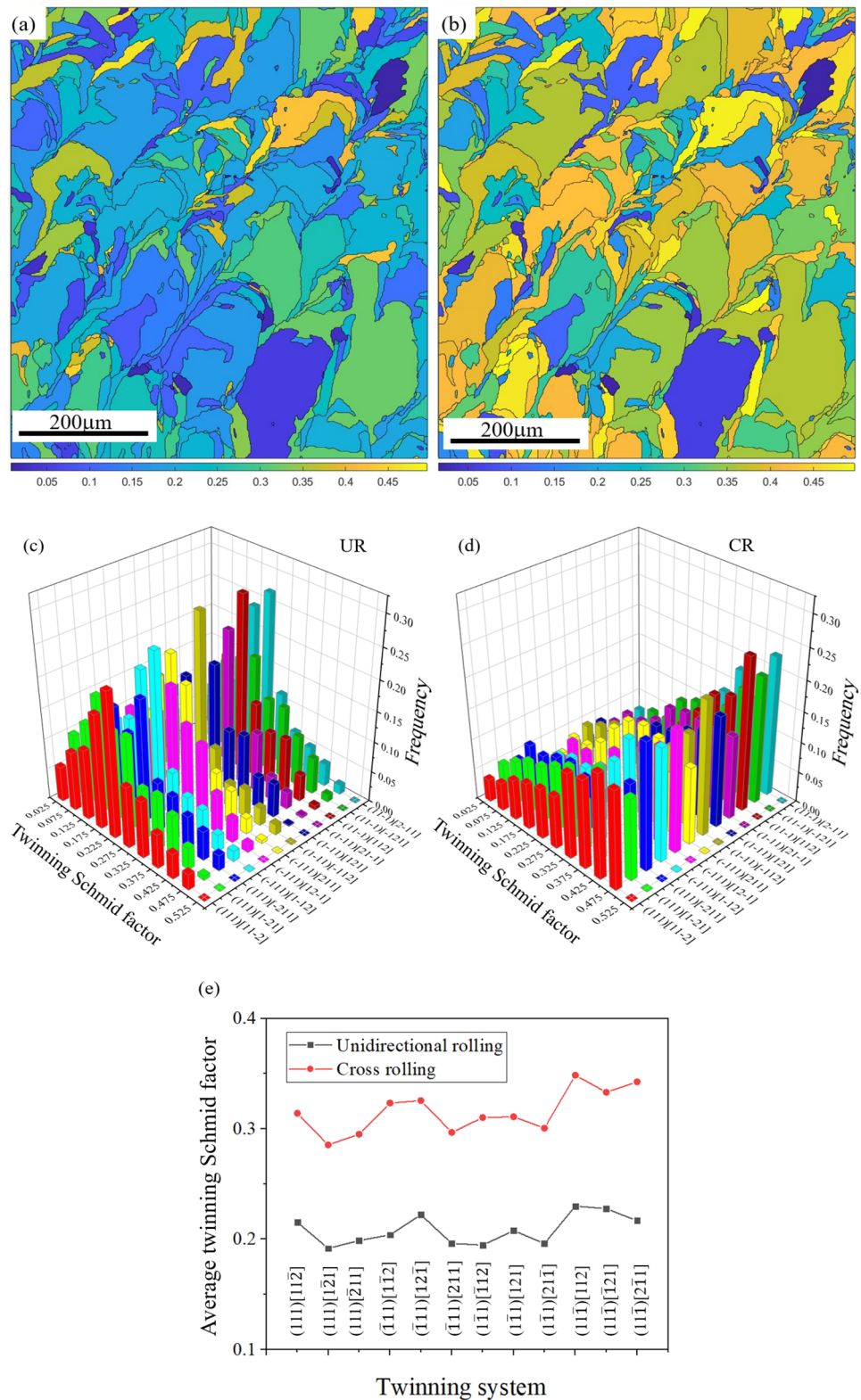


the formation of the deformation twins, adjacent planes are more likely to initiate additional partial dislocations. The twinned region widens and extends outward as the following twinning partial dislocations nucleate and spread outward from the twinning source [41]. Thus, the much higher density of deformation twins in 10% rolled AB samples than that of the HT samples can be explained by the higher amount of nucleation sites for deformation twinning resulting from the larger number of dislocation cells.

The substantially increased hardness in the ABC sample after 10% thickness reduction can be attributed to both high dislocation and twin density (Fig. 9b and c). Moreover, more

twinning systems along different directions in single austenite grains are activated in the ABC sample as compared to other samples (Figs. 4 and 5). The strengthening derived from the formation of deformation twins can be understood from the decreased effective mean free path for dislocation glide, which is also known as dynamic Hall-Petch effect [42]. More importantly, multiple TBs from different directions can effectively inhibit the dislocation motions [43, 44]. The higher hardness of the HTU sample than that of the HTC sample can be ascribed to the higher dislocation density. Nevertheless, the deformation twins are sparsely distributed in the matrix with relatively large spacing resulted

Fig. 10 Schmid factor map of AB 316 L to $(111)[112]$ twinning system under **a** UR and **b** CR. The color bar demonstrates the Schmid factor values. **c, d** Grain frequency of Schmid factors to twinning systems under UR and CR. **e** Average twinning Schmid factors to the twinning systems. (For interpretation of the references to color in this figure legend, the reader is referred to the web version of this article.)



from the lack of twinning nucleation sites in both HTU and HTC samples, which thus contribute little to the general work-hardening behavior [45]. Additionally, the dislocation glide and deformation twinning are mutually exclusive

deformation mechanisms at the initial deformation stage according to the Schmid law [46], i.e., the selection of the deformation mechanism is depending on the critical shear or twinning stress which is first reached at the external stress

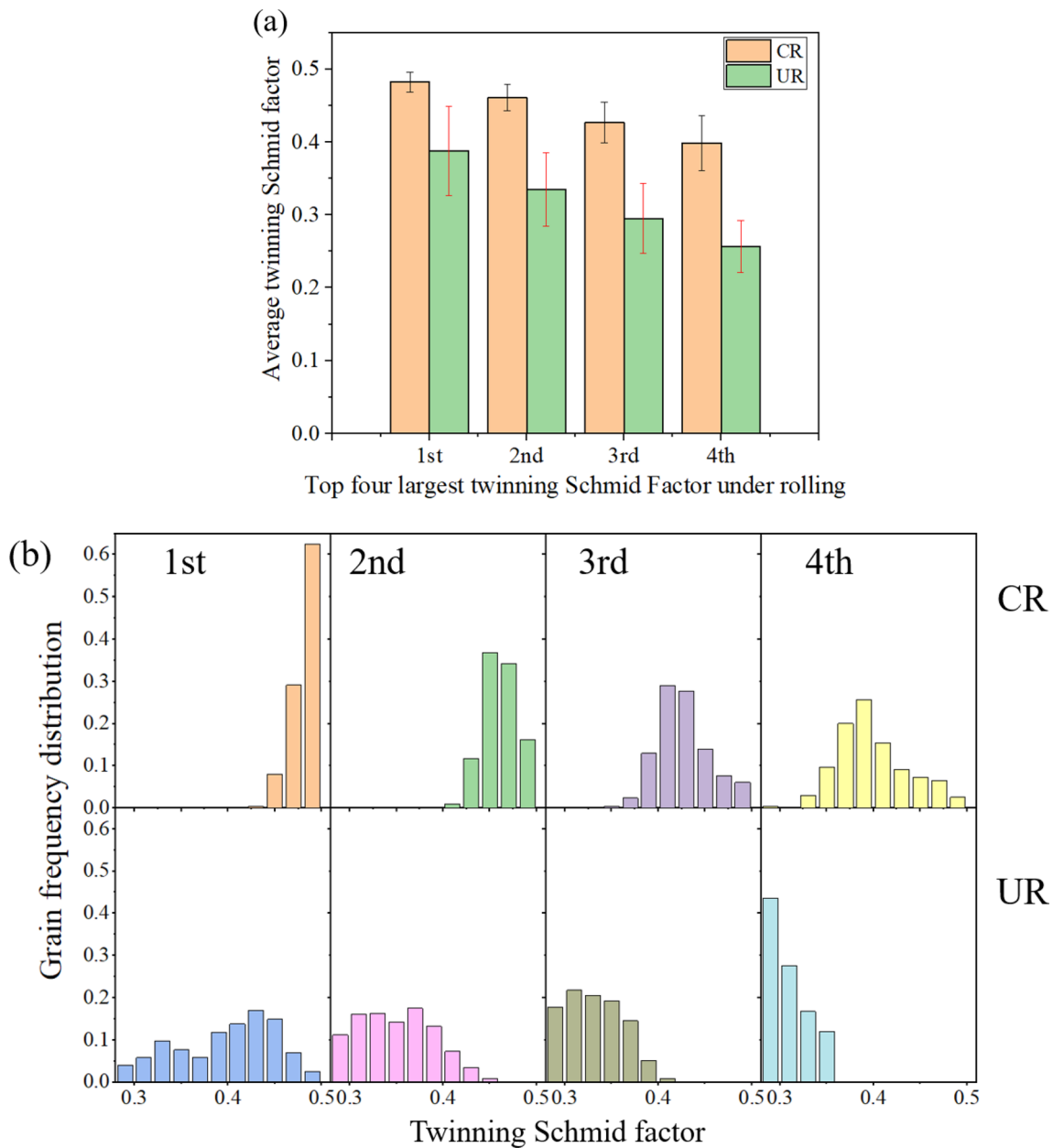


Fig. 11 **a** The top four largest average twinning Schmid factors in grains. **b** Grain frequency distribution to twinning Schmid factors under different rolling conditions

condition. At the thickness reduction of 30%, the dislocation and twin density of the ABC sample are higher than that of the ABU sample (Fig. 9c), and the average crystallite size is lower than that of the ABU sample (Fig. 9d), these factors contribute to a higher hardness of the ABC sample as compared to that of the ABU sample. As the thickness reduction increased to 50%, all samples share a similar twin density and average crystallite size according to the neutron diffraction analysis (Fig. 9d). Thus, the higher hardness of ABC sample after 50% thickness reduction as compared to other samples could be due to the relatively higher dislocation

density (Fig. 9c). The reason for the operation of deformation twins under different amounts of strains could be several folds. It has been shown that the twins are intersected and then smashed at a large deformation stage [36]. Moreover, the existing multiple twins can impede the formation of new twins [47]. In addition, grain rotation can take place at large plastic deformation and changes the Schmid factors for the activation of deformation twinning [48, 49]. Additionally, multi-directional deformation typically results in the annihilation of opposing dislocations that are initiated in different deformation directions [50]. These factors could make the

number of deformation twins in the present samples after different rolling conditions similar to a large deformation regime (50% thickness reduction) [16].

5 Conclusion

In summary, the deformation behaviors of AB and HT 316 L under unidirectional and cross rolling are systematically studied. A high-density of deformation twins with multiple systems is observed in crossly rolled AB 316 L at low thickness reduction (10%), along with a substantial hardness increment (108.6 HV, ~48.5%), which can be ascribed to the high density of twins and dislocations. The high twin density can be ascribed from the effectively raised twinning Schmid factors and initiation of twinning systems from different directions realized by cross rolling and may also be related to the dislocation cell boundaries of AB 316 L that provide many nucleation sites. The high-density of deformation twins with multiple systems have high dislocation storage ability and thus result in the high hardness at small deformation.

Acknowledgements B.B. He gratefully acknowledges the financial support from the National Natural Science Foundation of China (Grant No. U52071173), Science and Technology Innovation Commission of Shenzhen (Project No. JCYJ20210324120209026; KQTD2019092917250571) and Major Talent Programs of Guangdong Province (Contract No. 2019QN01C435). The authors would like to acknowledge the technical support from SUSTech Core Research Facilities and the general-purpose powder diffractometer (GPPD) of the China Spallation Neutron Source (CSNS), Dongguan, China for the neutron diffraction experiments.

Author Contributions XH: Methodology, Investigation, Data curation, Formal analysis, Writing. BBH: Supervision, Review & editing, Funding acquisition.

Data Availability The raw data required to reproduce these findings are available from the corresponding author of this paper. The processed data required to reproduce these findings are available from the corresponding author of this paper.

Declarations

Conflict of interest On behalf of all authors, the corresponding authors state that there is no conflict of interest.

References

1. S.H. Huang, P. Liu, A. Mokasdar, L. Hou, *Int. J. Adv. Manuf. Technol.* **67**, 1191–1203 (2012)
2. D. Herzog, V. Seyda, E. Wycisk, C. Emmelmann, *Acta Mater.* **117**, 371–392 (2016)
3. F.K. Yan, G.Z. Liu, N.R. Tao, K. Lu, *Acta Mater.* **60**, 1059–1071 (2012)
4. U.I. Thomann, P.J. Uggowitzer, *Wear* **239**, 48–58 (2000)
5. B. AlMangour, D. Grzesiak, J.-M. Yang, *J. Alloys Compd.* **706**, 409–418 (2017)
6. Y. Zhong, L. Liu, S. Wikman, D. Cui, Z. Shen, *J. Nucl. Mater.* **470**, 170–178 (2016)
7. L.F. Liu, Q.Q. Ding, Y. Zhong, J. Zou, J. Wu, Y.L. Chiu, J.X. Li, Z. Zhang, Q. Yu, Z.J. Shen, *Mater. Today* **21**, 354–361 (2018)
8. A. Rohatgi, K.S. Vecchio, G.T. Gray, *Metall. Mater. Trans. A* **32**, 135–145 (2001)
9. A.K. Agrawal, A. Singh, A. Vivek, S. Hansen, G. Daehn, *Mater. Lett.* **225**, 50–53 (2018)
10. L. Lu, Y. Shen, X. Chen, L. Qian, K. Lu, *Science* **304**, 422–426 (2004)
11. K. Lu, L. Lu, S. Suresh, *Science* **324**, 349–352 (2009)
12. G.G. Yapici, I. Karaman, Z.P. Luo, H.J. Maier, Y.I. Chumlyakov, *J. Mater. Res.* **19**, 2268–2278 (2004)
13. J.W. Simmons, *Mater. Sci. Eng. A* **207**, 159–169 (1996)
14. Q. Yu, L. Qi, K. Chen, R.K. Mishra, J. Li, A.M. Minor, *Nano Lett.* **12**, 887–892 (2012)
15. S. Mishra, K. Narasimhan, I. Samajdar, *Mater. Sci. Technol.* **23**, 1118–1126 (2007)
16. Y. Jiang, X. Zhou, X.Y. Li, *Mater. Sci. Eng. A* **822**, 141703 (2021)
17. L. Cui, S. Jiang, J. Xu, R.L. Peng, R.T. Mousavian, J. Moverare, *Mater. Des.* **198**, 109385 (2021)
18. T. Voisin, J.-B. Forien, A. Perron, S. Aubry, N. Bertin, A. Samanta, A. Baker, Y.M. Wang, *Acta Mater.* **203**, 116476 (2021)
19. L. Liu, Q. Yu, Z. Wang, J. Ell, M.X. Huang, R.O. Ritchie, *Science* **368**, 1347–1352 (2020)
20. P. Mercelis, J.P. Kruth, *Rapid Prototyp. J.* **12**, 254–265 (2006)
21. S.I. Wright, M.M. Nowell, D.P. Field, *Microsc. Microanal.* **17**, 316–329 (2011)
22. A.A. Gazder, A.A. Saleh, E.V. Pereloma, *Scr. Mater.* **65**, 560–563 (2011)
23. K. Renard, P.J. Jacques, *Mater. Sci. Eng. A* **542**, 8–14 (2012)
24. M. Calcagnotto, D. Ponge, E. Demir, D. Raabe, *Mater. Sci. Eng. A* **527**, 2738–2746 (2010)
25. M. Wojdyr, *J. Appl. Cryst.* **43**, 1126–1128 (2010)
26. T. Ungar, S. Ott, P.G. Sanders, A. Borbely, J.R. Weertman, *Acta Mater.* **46**, 3693–3699 (1998)
27. Y.Z. Li, M.X. Huang, *Acta Metall. Sin.* **56**, 487–493 (2020)
28. X. Zhang, P. Kenesei, J.-S. Park, J. Almer, M. Li, *J. Nucl. Mater.* **549**, 152874 (2021)
29. Y.Z. Li, S.L. Zhao, S.H. He, C.P. Huang, M.X. Huang, *Int. J. Plast.* **155**, 103334 (2022)
30. T. Ungár, *Mater. Sci. Eng. A* **309–310**, 14–22 (2001)
31. H. Wilhelm, A. Paris, E. Schafner, S. Bernstorff, J. Bonarski, T. Ungar, M.J. Zehetbauer, *Mater. Sci. Eng. A* **387–389**, 1018–1022 (2004)
32. B.E. Warren, *Progr. Met. Phys.* **8**, 147–202 (1959)
33. T. Ungar, I. Dragomir, A. Revesz, A. Borbely, *J. Appl. Cryst.* **32**, 992–1002 (1999)
34. M. Shamsujjoha, S.R. Agnew, J.M. Fitz-Gerald, W.R. Moore, T.A. Newman, *Metall. Mater. Trans. A* **49**, 3011–3027 (2018)
35. Z.Y. Liang, X. Wang, W. Huang, M.X. Huang, *Acta Mater.* **88**, 170–179 (2015)
36. C.S. Hong, N.R. Tao, X. Huang, K. Lu, *Acta Mater.* **58**, 3103–3116 (2010)
37. J.R. Luo, A. Godfrey, W. Liu, Q. Liu, *Acta Mater.* **60**, 1986–1998 (2012)
38. J. Jeong, Y. Lee, J.M. Park, D.J. Lee, I. Jeon, H. Sohn, H.S. Kim, T.-H. Nam, H. Sung, J.B. Seol, J.G. Kim, *Additive Manuf.* **47**, 102363 (2021)
39. K.M. Rahman, V.A. Vorontsov, D. Dye, *Acta Mater.* **89**, 247–257 (2015)
40. J. Jung, J.I. Yoon, J.G. Kim, M.I. Latypov, J.Y. Kim, H.S. Kim, *Npj Comput. Mater.* **3**, 21 (2017)

41. B.Q. Li, M.L. Sui, S.X. Mao, *J. Mater. Sci. Technol.* **27**, 97–100 (2011)
42. B.C. De Cooman, Y. Estrin, S.K. Kim, *Acta Mater.* **142**, 283–362 (2018)
43. X.W. Liu, L.G. Sun, L.L. Zhu, J.B. Liu, K. Lu, J. Lu, *Acta Mater.* **149**, 397–406 (2018)
44. L.L. Zhu, H.N. Kou, J. Lu, *Appl. Phys. Lett.* **101**, 081906 (2012)
45. Z.C. Luo, M.X. Huang, *Scr. Mater.* **142**, 28–31 (2018)
46. M. Arminjon, *Texture Microstruct.* **14**, 1121–1128 (1991)
47. S.-G. Hong, S.H. Park, C.S. Lee, *Acta Mater.* **58**, 5873–5885 (2010)
48. P. Yang, Q. Xie, L. Meng, H. Ding, Z. Tang, *Scr. Mater.* **55**, 629–631 (2006)
49. S.S. Cai, X.W. Li, N.R. Tao, *J. Mater. Sci. Technol.* **34**, 1364–1370 (2018)
50. D.H. Ahn, M. Kang, L.J. Park, S. Lee, H.S. Kim, *Mater. Sci. Eng. A* **684**, 567–576 (2017)

Publisher's Note Springer Nature remains neutral with regard to jurisdictional claims in published maps and institutional affiliations.

Springer Nature or its licensor (e.g. a society or other partner) holds exclusive rights to this article under a publishing agreement with the author(s) or other rightsholder(s); author self-archiving of the accepted manuscript version of this article is solely governed by the terms of such publishing agreement and applicable law.